Received 12 July 2020; revised 12 August 2020; accepted 16 September 2020. Date of publication 18 September 2020; date of current version 5 October 2020.
The review of this article was arranged by Editor P. Pavan.

Digital Object Identifier 10.1109/JEDS.2020.3024669

TCAD-Machine Learning Framework for Device Variation and Operating Temperature Analysis With Experimental Demonstration

HIU YUNG WONG [1] (Senior Member, IEEE), MING XIAO [2], BOYAN WANG [2], YAN KA CHIU [1], XIAODONG YAN [3], JIAHUI MA [3], KOHEI SASAKI [4], HAN WANG [3] (Senior Member, IEEE), AND YUHAO ZHANG [2] (Member, IEEE)

1 Department of Electrical Engineering, San Jose State University, San Jose, CA 95112, USA
2 Virginia Polytechnic Institute, State University, Blacksburg, VA 24060, USA
3 Ming Hsieh Department of Electrical Engineering, University of Southern California, Los Angeles, CA 90089, USA
4 Development Department, Novel Crystal Technology Inc., Sayama 3501328, Japan

CORRESPONDING AUTHORS: H. Y. WONG, H. WANG, AND Y. ZHANG (e-mail: hiuyung.wong@sjsu.edu; han.wang.4@usc.edu; yhzhang@vt.edu)

(Hiu Yung Wong, Ming Xiao, Boyan Wang, and Yan Ka Chiu contributed equally to this work.)

ABSTRACT This work, for the first time, experimentally demonstrates a TCAD-Machine Learning (TCAD-ML) framework to assist the analysis of device-to-device variation and operating (ambient) temperature without the need of physical quantities extraction. The ML algorithm used in this work is the Principal Component Analysis (PCA) followed by third order polynomial regression. After calibrated to limited 'expensive' experimental data, 'low cost' TCAD simulation is used to generate a large amount of device data to train the ML model. The ML was then used to identify the root cause of device variation and operating temperature from any given experimental current-voltage (I-V) characteristics. We applied this framework to study the ultra-wide-bandgap gallium oxide (Ga_2O_3) Schottky barrier diode (SBD), an emerging device technology that holds great promise for temperature sensing, RF, and power applications in harsh environments. After calibration, over 150,000 electrothermal TCAD simulations are performed with random variation of physical parameters (anode effective work function, drift layer doping, and drift layer thickness) and operating temperature. An ML model is trained using these TCAD data and we found 1,000-10,000 TCAD data can train an accurate machine. We show that without physical quantities extraction, performing PCA is essential for the TCAD trained ML model to be applicable to analyze experimental characteristics. The physical parameters and temperatures predicted by the ML model show good agreement with experimental analysis. Our TCAD-ML framework shows great promise to accelerate the development of new device technologies with a significantly more efficient process of material and device experimentation.

INDEX TERMS TCAD simulation, machine learning, variation, principal component analysis, ultra-wide bandgap, gallium oxide.

I. INTRODUCTION

Machine learning (ML) has recently gained increased attention for applications in semiconductor manufacturing, such as the etch anomaly analysis [1], lithographic hotspot detection [2] and optical proximity correction [3]. On the other hand, wafer-level device variation analysis is critical for the development of any nascent semiconductor technologies. These variations may be material-related and process-related. Today's analysis practices mostly rely on extensive device and material characterizations. Many of these characterizations (e.g., cross-sectional microscopic inspection) are destructive, prohibitively costly, and time-consuming to implement for every device in a wafer. An ML assisted variation analysis based on device electrical characteristics is highly desired to allow for more efficient material and device experimentation.

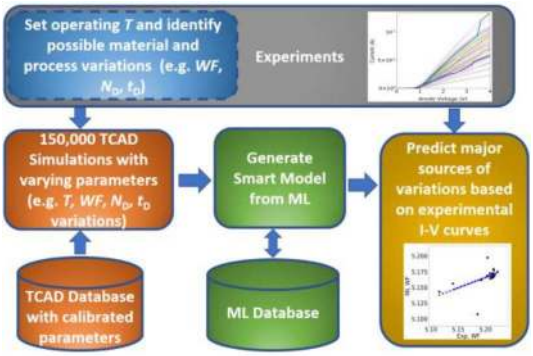

FIGURE 1. **Flow chart diagram of the proposed TCAD-Machine Learning framework. All components are demonstrated in this article except the ML Database which stores previously trained ML algorithms.**

Recently, it has been proposed that the TCAD simulation based on well-calibrated parameters can be used to generate enough data for ML in variation and failure analysis [4], [5]. Reference [6] proposed to use ML to replace TCAD simulation for device variation analysis and [7] used ML to replace TCAD simulation to for power device breakdown prediction. However, none of these frameworks has been verified with experimental data, which are usually non-ideal due to equipment limitation, extra variables, and measurement noise. Moreover, physical quantities extraction (e.g., extraction of threshold voltage and sub-threshold slope in I-V characteristics) was required in the ML frameworks that were reported in [5] and [6], which limits their applicability.

In this work, we for the first time demonstrate an ML-based TCAD framework with experimental data verification. Fig. 1 shows the flow chart diagram of the proposed framework. As a feasibility demonstration, our ML-TCAD framework was applied to analyze the variation of gallium oxide (Ga_2O_3) Schottky barrier diodes (SBDs) fabricated on 2-inch wafers and shows an agreement with experiment with no need of physical quantities extraction. Note that this framework is used to study the device-to-device variation instead of performing statistical variation analysis like in [10]. We also showed that TCAD data can be generated accurately and at *low-cost* (150,000 simulations in 2 weeks on 1 server), and studied the minimum amount of TCAD data that are required to train an accurate ML model for the analysis of experimental data. This framework allows the use of various types of ML algorithms, from the simplest linear regression to more sophisticated neural network [8], [9]. Principal Component Analysis (PCA) followed by third order polynomial regression is used in this article.

We believe this framework is particularly useful at the nascent stage of any technology development. This is because a large amount of training data is required to develop a good ML model. However, for immature technology, there are not enough wafers but can be complemented by TCAD simulations. Meanwhile, the results presented in this work show great promise for applying the TCAD-ML framework onto more mature semiconductors and commercially available device technologies.

As an emerging ultra-wide-bandgap semiconductor, Ga_2O_3 has recently emerged as a promising material for high-temperature sensing, RF, and power applications, due to its ultra-wide bandgap (~4.8 eV), the availability of large-diameter wafers, and superior thermal stability when compared to Si, SiC and GaN [11], [12]. Polycrystalline Ga_2O_3 sensors have been demonstrated to operate at over 500°C [8]. Single crystalline Ga_2O_3 power devices with hundreds of volts breakdown voltage have been demonstrated to function at 350°C [13]. However, as a nascent material and device technology, Ga_2O_3 electronics suffer from considerable epitaxy and process non-uniformity and therefore require extensive variation analysis in its development. This makes the Ga_2O_3 device an excellent platform for experimental verification of our TCAD-ML framework. On the other hand, the successful application of our ML-TCAD framework in Ga_2O_3 shows great promise to expedite its commercialization and applications.

Due to the high-temperature potentials of Ga_2O_3 devices, we also used the same framework to analyze the device operating (ambient) temperature based on its experimental I-V curves. Our framework shows the feasibility to predict the device operating temperature, which obviates the use of special temperature-sensing circuits in high-temperature Internet-of-Things (IoTs) applications or costly thermal characterizations such as thermoreflectance and Raman spectroscopy during device characterizations.

Besides the demonstration of the ML-TCAD framework, this work also provides new device insights into Ga_2O_3 devices. The accurate TCAD calibration and simulations have been performed for vertical Ga_2O_3 power SBDs. For the first time, both Ge-doped and Si-doped Ga_2O_3 temperature-dependent electron mobilities are calibrated for the Philips Unified Mobility Model in TCAD in a wide temperature range. The incomplete ionization of dopants was also implemented in Ga_2O_3 and achieved a good agreement with the experiment.

II. EXPERIMENT

Fig. 2(a) shows the schematic of the Ga_2O_3 SBDs fabricated on 2-inch free-standing (001) Ga_2O_3 wafers. The wafer epitaxial structure consists of a Si-doped n-Ga_2O_3 drift layer grown on a commercial 2-inch n^+-Ga_2O_3 (Sn-doped) substrate by Halide Vapor Phase Epitaxial (HVPE). The substrate has good uniformity in thickness and resistivity. The thickness (t_D) and net donor concentration (N_D) of the n-Ga_2O_3 drift layer were measured at five spots across the 2-inch wafer using electrochemical capacitance-voltage (ECV) and secondary ion mass spectrometry (SIMS), respectively. Fig. 2 (b) shows the SIMS profile for Si ion concentration measured at two spots, where the increase in Si concentration marks the interface between the drift region and substrate. Note the donor in the drift region not only comes

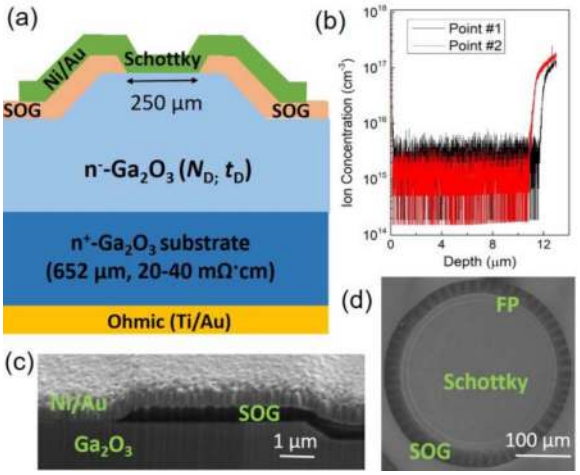

FIGURE 2. (a) Schematic of the fabricated vertical Ga_2O_3 power Schottky barrier diodes; (b) An exemplary illustration of the drift layer thickness at two spots on the wafer determined by the Si profile measured by secondary ion mass spectrometry. (c) Cross-sectional scanning electron microscopy (SEM) image of the field plate region; (d) Top-view SEM image of the fabricated device.

TABLE 1. PhuMob parameters calibrated in TCAD against experiment. The symbols are the same as those in [17, Tab. 1]. θ is the exponent of temperature dependence due to lattice scattering.

	As in Si	Si in Ga_2O_3	Ge in Ga_2O_3
μ_{max} ($cm^2/V{\cdot}s$)	1.42×10^3	123	115
μ_{min} ($cm^2/V{\cdot}s$)	52.2	80	0
Θ	2.29	1.8	1.65
$N_{ref,1}$ (cm^{-3})	9.68×10^{16}	2×10^{17}	5.68×10^{18}
α_1	0.68	0.9	0.68

from Si but also from other impurities such as O, so the measured N_D by ECV is higher than the measured Si concentration by SIMS. From the measurement across these spots, a relatively large variation in t_D (7.5 $\sim$ 11.9 μm) and N_D (2.1 $\sim$ 4.6 $\times$ 10^{16} cm^{-3}) was found for the drift layer. Note these techniques are difficult to measure the t_D and N_D in every fabricated device, as ECV and SIMS are both destructive and have a large spatial size (hundreds of micron meters) for each measurement point.

Over 55 field-plated power Ga_2O_3 SBDs were fabricated across the wafer, with the cross-sectional and top-view scanning electron microscopy (SEM) images shown in Fig. 2(c) and (d). The device fabrication starts with mesa etch, followed by the deposition of spin-on-glass (SOG) as the field-plate (FP) dielectrics. A blanket backside Ohmic contact was formed by Ti/Au deposition followed by a 470°C annealing. The SOG was then opened through wet etch, followed by the metal deposition to form Schottky contacts and field plates. More details of device fabrication are described in [13] and [14]. Before the Schottky metal deposition, the wafer was cut into small samples, and different surface chemical treatment (water, hydrochloric acid, buffered oxide etch) were applied to intentionally introduce the variations in the Schottky barrier height [15]. From our experimental device

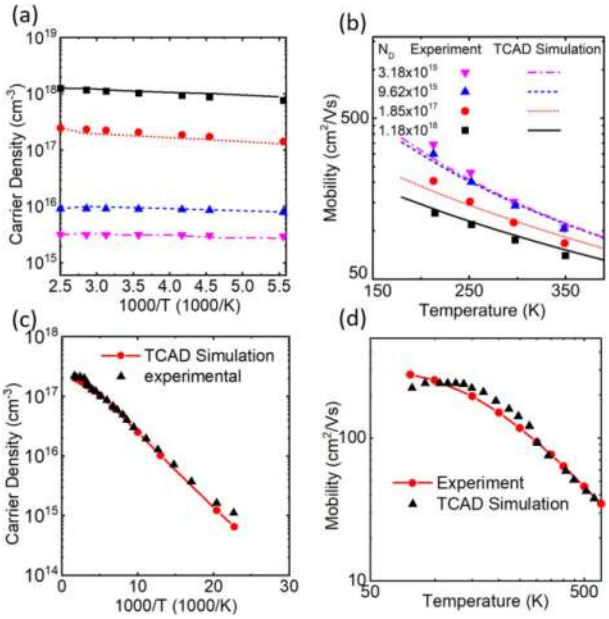

FIGURE 3. Comparison of experimental [18], [20] and TCAD PhuMob electron mobility and free carrier concentration data in Si-doped ((a)-(b)) and Ge-doped ((c)-(d)) Ga_2O_3.

analysis, the different surface treatment creates the variation in effective metal workfunction in the range of ~0.1eV, rendering a good representative of the effective Schottky barrier height variations due to (one or multiple) mechanisms such as metal workfunction uncertainties, surface doping and roughness variations, and interface states uncertainties. Meanwhile, the variation in the Schottky barrier height (or effective metal workfunction) can be measured with non-destructive and low-cost electrical technique to check the performance of the framework. The fabricated Ga_2O_3 SBDs have a circular anode with a diameter of 250 μm.

The I-V characteristics of the 55 fabricated devices at different locations of the 2-inch wafer were collected, where each device was measured from 300 K to 510 K, with the chuck temperature carefully calibrated by a thermal camera. Each I-V measurement is performed from a reverse bias of −10 V to a forward bias of 4 V.

III. TCAD CALIBRATION AND SIMULATIONS

TCAD Sentaurus is used in this study [16]. Since Ga_2O_3 is an emerging material, simulation models and parameters need to be chosen and calibrated carefully. Philips Unified Mobility Model (PhuMob) [17] is calibrated for Si-doped Ga_2O_3 experimental data (Fig. 3(a)) [18]. The incomplete ionization model is turned on. Doping dependent activation energy model is used [16],

$$E_D = E_{D,0} + \alpha N^{1/3} \tag{1}$$

where E_D is the activation energy of the dopant, $E_{D,0}$ is the activation energy when the dopant concentration approaches zero, α is a constant and N is the doping concentration in cm^{-3}. For the best fitting to experimental data in [18],

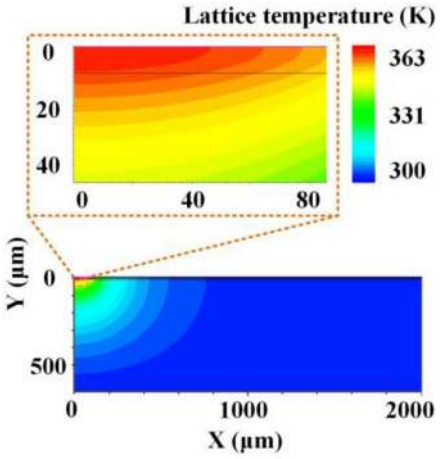

FIGURE 4. Simulated temperature distribution at a forward bias of 4 V in the whole simulated structure with cylindrical coordinates (identical to total piece size) and in the zoomed-in anode region.

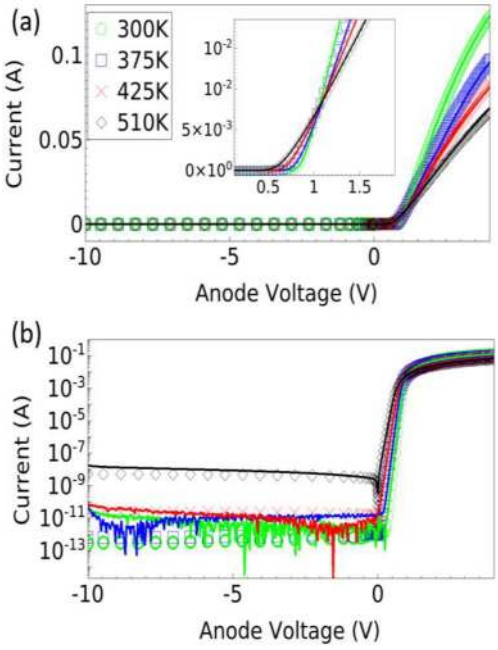

FIGURE 5. Experimental (lines) and TCAD simulated (markers) I-V curves in (a) linear and (b) log scale at different temperatures. Inset shows the I-V curves in the turn-on region.

$E_{D,0} = 52$ meV and $\alpha = 3.4 \times 10^{-8}$ eV·cm are used for Si. This is consistent with the literature results in [18], [19] and gives excellent agreement with experimental free carrier densities obtained from Hall measurement in [18] (Fig. 3(b)). To increase the confidence of the appropriateness of our calibration methodology, the TCAD model is also calibrated against Ge-doped Ga_2O_3 experimental data [20] and excellent agreement is also achieved in both mobility and free carrier concentrations from 77K to 550K (Fig. 3(c) and (d)). The calibrated parameters for PhuMob in Ga_2O_3 are shown in Table 1 together with the parameters in Si for comparison. Only parameters different from Silicon are shown in

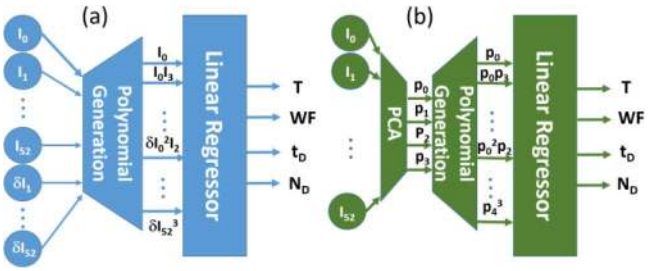

FIGURE 6. Schematic of the ML algorithm used in this study. (a) 3rd order polynomial generation for "with physical quantities extraction" and (b) PCA followed by 3rd order polynomial generation for "without physical quantities extraction". Meanings of the symbols are explained in Table 3.

TABLE 2. Means and ranges of parameters and temperature variation in TCAD simulations.

	Mean	Range
WF (eV)	5.09	0.1
T (K)	400	100
t_D (μm)	9	4
N_D (cm^{-3})	4×10^{16}	3×10^{16}

Table 1. Θ is the exponent of temperature dependence due to lattice scattering.

Due to the low thermal conductivity of Ga_2O_3, device self-heating and three-dimensional (3-D) heat dissipation in the whole sample need to be considered. Thermal conductivity along the [001] axis is selected based on [21]. Thermodynamic model is turned on. A half 2-D cross-section of the experimental structure is simulated using a cylindrical coordinate, which performs essentially a 3-D simulation of the SBD in a 0.5 mm^2 sample (Fig. 4). This obviates the need for lump thermal resistance calibration. This is because if limited domain or pure 2D simulation is used, in order to capture the thermal resistance due to the 3D substrate, an effect lumped thermal resistor needs to be attached and calibrated. It can be seen that self-heating occurs mostly in the drift layer (top ~10 μm) below the Schottky contact.

The simulation deck is calibrated against the experimental results of the selected diode at various operating temperatures from 300 K to 510K. As shown in Fig. 5, an excellent agreement in experimental and simulated I-V characteristics has been achieved in the reverse bias, forward bias, and device turn-on regions in both the linear and log scales.

IV. MACHINE LEARNING

By using the calibrated TCAD simulation deck, three physical parameters, effective work function (*WF*, i.e., the work function that takes into account the Schottky barrier height variation), t_D, N_D, and the operating (ambient) temperature T are varied randomly. Table 2 shows the means and ranges of the parameters. Parameters are generated uniformly within the $mean \pm range$ of the corresponding parameter. For example, T is varied between 300K and 500K. So $mean = 400K$ and $range = 100K$. The ranges are set to be larger than the

TABLE 3. Explanations of the symbols of the ML algorithms in Fig. 6.

	Range of i	Meaning
I_i	0-51	Discretization of the current value of the *IV* curve
δI_i	1-51	I_i-I_{i-1}
p_i	0 - 3	Extracted Principal Components

expected variation of the parameters. Meanwhile, all experimental I-V characteristics are from the "functional" devices with no obvious failure. The *WF* variation is mainly produced by various surface treatment mentioned in Section II. The consideration of the *WF* variation is essential to mimic the barrier height inhomogeneity widely reported in Ga_2O_3 SBDs [13], [22], [23].

150,000 devices are generated in Sentaurus Structure Editor [24] with these varied parameters and their I-V curves are obtained through device simulation in SDevice [16]. Supervised learning ML is used [8]. The I-V curves are the input features and the varied parameters and temperature (*W, t_D, N_D, T*) are the labels/outputs. 80% is used for the ML model training and 20% for validation. All the simulations are completed in 2 weeks on 1 single server (2 Fourteen-Core Intel Xeon Processor E5-2690 v4 2.60GHz with hyperthreading), which is virtually impossible to obtain experimentally. This demonstrates that TCAD can be used to generate data to augment the ML with a very low cost.

The I-V curves are discretized to 52 points from V = 0V to V = 4V as input features for ML. Polynomial regression of the 3rd order is used to capture the non-linear dependence of outputs on input features. Fig. 6 shows two types of algorithms are tested for with and without physical quantities extraction. The meanings of the symbols are shown in Table 3. Terms up to third order are generated as the input (e.g., I_0 (first order), I_0I_{32} (second order), $I_1I_{32}^2$ (third order)) to the linear regression and is regressed against the output (*T, W, t_D, N_D*).

Higher order polynomial regression (up to 5th order) and neural networks (NNs) were also explored in this work. For example, a neuron network with 3 hidden layers, each with 32, 16, and 10 internal nodes, respectively, have been applied to the dataset. However, in general, they were found to produce a worse result and require much longer training time than 3rd order polynomial regression. This is probably due to overfitting. This also indicates that a more substantial effort might be needed to optimize the NNs, which may offset the benefit of ML without physical quantities extraction. While the underlying mathematical mechanisms of the failure in NNs will be scrutinized in our future work, only 3rd order polynomial regression is discussed in this work.

A. WITH PHYSICAL QUANTITIES EXTRACTION

Based on the knowledge in semiconductor physics, it is expected that the slope of the I-V curve in the subthreshold region represents *nkT/q* and the maximum change of slope represents the turn-on voltage, which is related to *WF*. Therefore, changes of the current at each voltage bias (δI_i) are also computed as the input features as shown in Fig. 6(a), where $\delta I_i = I_i - I_{i-1}$ for $i = 1$ to 52. Note that, even though physical quantities extraction is required in this case, it is intentionally minimized. It is important to avoid too much human intervention as in traditional inverse designs reported in [25]–[28]. 3rd order polynomials are then generated from *I* and *dI* for machine learning. Without d*I*, machine training is more difficult and more data are required to get the same level of accuracy. Fig. 7 shows the training (on 120,000 I-V curves) and testing (on 30,000 I-V curves) results. The trained machine is able to predict the three physical parameters and device operating temperature accurately for any given *I-V* curves.

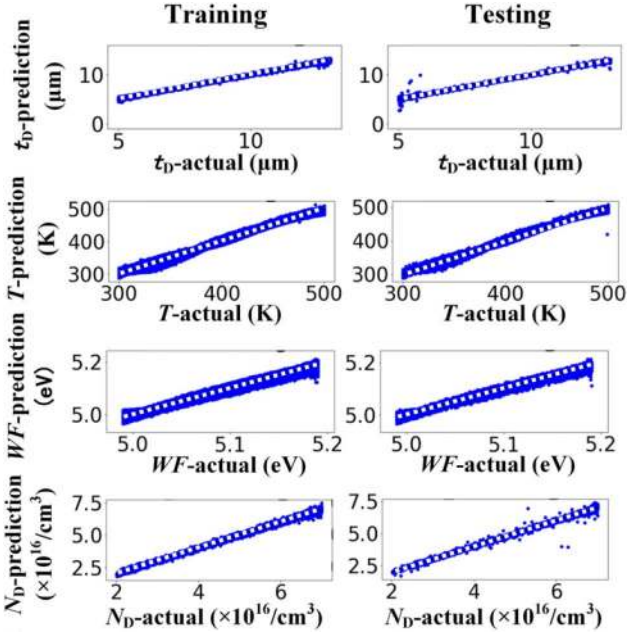

FIGURE 7. Training results of 120,000 data points (left) and testing results of 30,000 data points (right). The white dotted line shows the reference that the predicted values agree with the actual ones.

Fig. 8 shows the normalized root mean squared errors (RMS) for different parameters as a function of training data set size. The RMS error is normalized to the range of variation (see Table 2) of the corresponding parameter used to generate the data set. For example, WF is generated randomly within the range of 5.09 eV±0.1 eV. The RMS is normalized to 0.1 eV. Therefore, 7% error refers to about 0.007eV of RMS. Fig. 8 shows that only 10,000 training data is required to attain less than 10% of the variation range for t_D and N_D. This means that sufficient TCAD data can be generated in less than 2 days to train the machine. For *T* and *WF*, even with only 1,000 training data, the errors are still very low. Therefore, if one is only interested in predicting *T* and *WF*, only 1,000 TCAD data needs to be generated and it takes less than 4 hours.

Therefore, a machine is trained successfully to predict the structural parameters (*WF*, t_D, and N_D) and operating condition (*T*) for any given ideal *I-V*. Here 'ideal' means

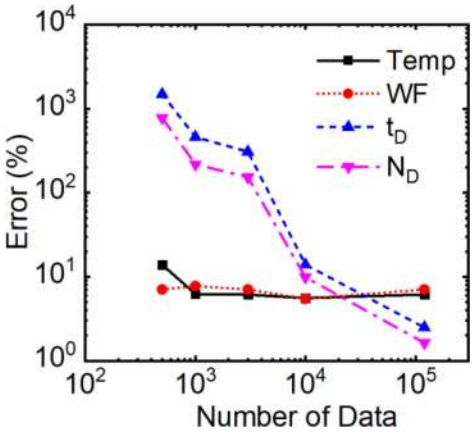

FIGURE 8. Testing data set root-mean-squared errors normalized to data variation range as a function of training data set size.

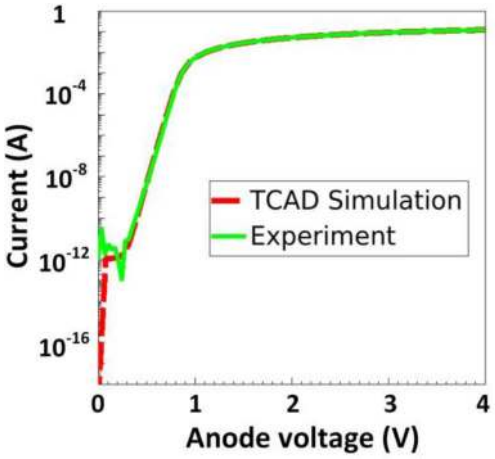

FIGURE 9. Experimental I-V curve and calibrated TCAD I-V curve showing big difference at V < 0.4 V due to measurement equipment limitation, despite very good overall calibration.

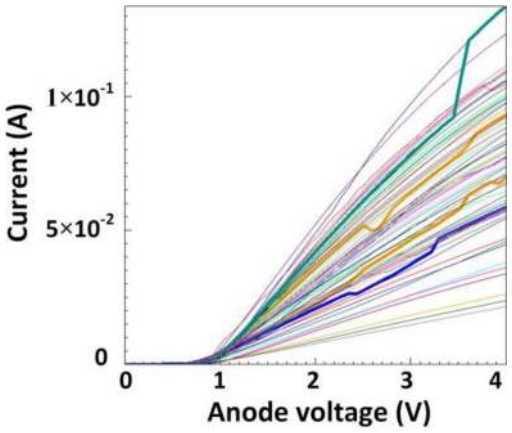

FIGURE 10. Some experimental I-V curves from the 55 devices collected at various temperatures. Some typical abnormal I-V curves are highlighted.

the *I-V's* are created by only varying these four variations (T, WF, t_D, and N_D). This will not be the case in experiment because there are other variations and noises which will affect the *I-V's*. This is an example of an *inverse design* problem [26]–[29] which can also be used for defect analysis and reverse engineering.

The TCAD trained machine is then used to predict the device parameters from experimental *I-V* curves. However, the result is found to be quite unsatisfactory. For example, while the TCAD simulated data matches the experimental data very well in Fig. 9 (the only visual discrepancy is the region where $V_{anode} < 0.4V$, due to noise and equipment limitation in the experimental curve) and the machine can predict the device parameter and operating temperature very well from the TCAD data (Fig. 7), it cannot predict the parameters and temperature well based on the given experimental I-V curve. While one can exclude the data in the voltage range below 0.4V in the training to avoid this problem, it is not desirable because there will be too much human intervention.

B. WITHOUT PHYSICAL QUANTITIES EXTRACTION

Ideally, a smart machine should be trained without the need of physical quantities extraction. Moreover, experimental I-V curves contain more variables than the ones considered in TCAD simulations and the measurement accuracy may be limited by equipment capability (such as noise). These factors can result in the failure of TCAD trained machine when it uses experimental I-V curves to predict physical parameters and operating temperature, such as the case in Fig. 9. Moreover, due to the immature process technology, such as contact issues, some I-V curves show anomalies (e.g., current humps, as shown in Fig. 10), which leads to unsatisfactory prediction.

To make the methodology applicable to experimental data and obviate the requirement of physical quantities extraction, we propose to perform Principal Components Analysis (PCA) on the input I-V curves before polynomial regression, as shown in Fig. 6(b) [8]. Four principal components are used because the TCAD data are generated by varying 4 parameters (i.e., WF, t_D, N_D and T). It is found that the robustness of the machine can be enhanced significantly. After the machine is trained using the TCAD-generated I-V curves with PCA (Fig. 6(b)), it is applied to 55 experimental I-V curves measured on various devices under different temperatures (Fig. 10) to predict the physical parameters of the devices. In Fig. 11, it shows the performance (i.e., prediction of the 4 parameters based on experimental *I-Vs* in Fig. 10) of the machine trained with (black) and without (red) PCA. The x-axes represent the experimental *I-V*'s. Since the experimental IV are from devices not related to each other, x-axes are not labeled but each *I-V* is placed on the same location of the axes of the 4 graphs. It is fond that with PCA, the machine is able to predict the physical parameters and operating temperature of all the experimental I-V curves in Fig. 10 to be within the expected range (black) while many from "without PCA" (red) are out of the expected range or even plotting range.

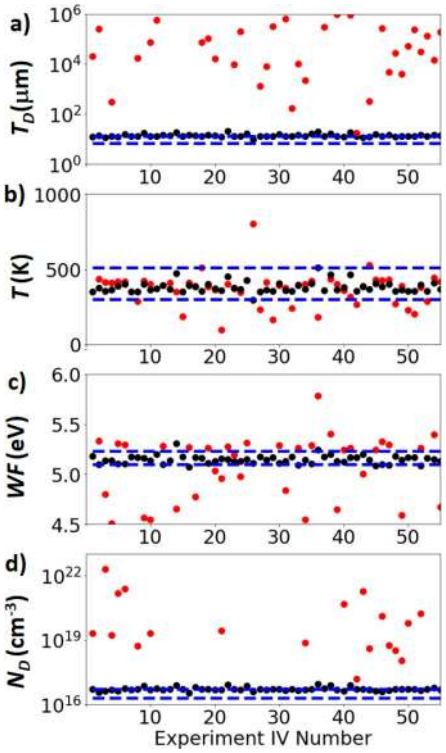

FIGURE 11. Prediction of experimental device parameters with (black) and without (red) PCA. Blue dash lines show the expected boundaries of the parameters based on physical analysis. Some red markers (without PCA) cannot be shown because they are outside of the plotting ranges. Each experimental *IV* from Fig. 10 is represented on the x-axes.

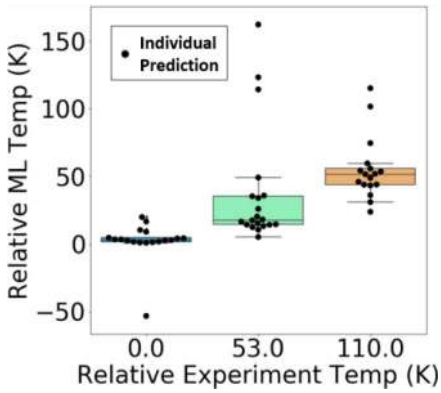

FIGURE 12. Seaborn boxplot of the prediction of device ambient temperature (*T*) by ML as a function of experiment temperature. Each dot represents the result of one experiment.

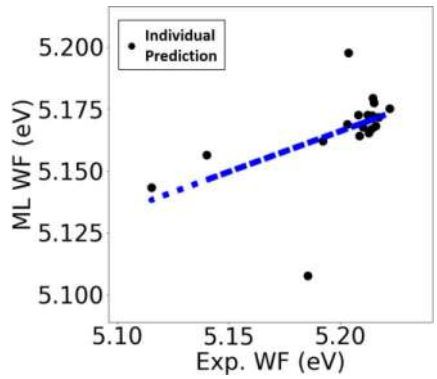

FIGURE 13. Prediction of *WF* using ML versus the experimentally extracted *WF*. Devices are measured at room temperature. Blue dashed line is the fitting curve.

Since the operating temperature of each device is known from the chuck temperature calibrated by thermal camera and device *WF* can be extracted by electrical methods (e.g., from the sub-threshold region of the forward I-V curve based on the thermal emission model [13], [29]), the ML predicted *T* and *WF* can be plotted against the known values of all devices. Fig. 12 shows that our ML model can predict the operating temperature in agreement with the actual temperature trend. Fig. 13 shows that the machine can predict the relative *WF* in agreement with the extracted *WF* trend from device experimental data using the device physics. Although the prediction of the absolute values is not perfect, provided the non-ideality of many of the experimental I-V curves shown in Fig. 10 and the co-existence of other unknown variations, the proposed TCAD ML framework has successfully provided statistically meaningful information on the physical properties of the Ga_2O_3 devices without the need for expensive and destructive physical characterizations. Most importantly, *no physical quantities extraction is required to extract physical quantities from IV curves as input features for ML.*

V. SUMMARY

We demonstrated by using TCAD simulation with well-calibrated parameters and appropriate models, a huge amount of electrical characteristic data can be generated for machine learning. The trained machine can then be used to predict the device parameters from any given experimental I-V curve. It should be noted that ML is a statistical process. Therefore, it is impossible to have 100% accuracy in predicting experimental device parameters. Indeed, for yield improvement and major defect source discovery in emerging semiconductor technology development, it is not necessary to have 100% accuracy.

A key advancement of our framework is to demonstrate that with PCA, the TCAD data trained machine can give statistically meaningful predictions of the device parameters. This framework is also robust as proved by the fact that *even the experiment data is very noisy and affected by many more known and unknown variables, the framework can still predict the trend of device parameters well*. Moreover, this framework *obviates the need for a large amount of experimental data for ML*, which is usually not available and prohibitively costly in any new semiconductor device technology development. Therefore, this framework relaxes the need for the extensive and costly device and material characterizations in the device variation analysis and is believed to be widely applicable to many new device technologies.

Similarly, such methodology can be used to predict the device operating temperature based on experimental I-V curves and obviates the need for special circuitry for temperature monitoring (particularly in harsh environments, the circuit would also require bulky and expensive cooling systems). Although the predicted temperature is not exactly the same as the experimental temperature, mainly due to the noises present in experimental data, our results, being the first experimental demonstration, have shown the feasibility of using TCAD augmented ML to assist in monitoring the device operating conditions.

Finally, our framework may be considered as one kind of inverse design. Compared to other inverse design using TCAD [25]–[28], our framework requires no physical quantities extraction and no complex optimizer (only simple 3rd order polynomial and PCA). The TCAD-based inverse design has been proposed for many years but it is still far away from a wide industrial adoption, probably due to the need for too much domain expertise in both data processing/selection and optimizer optimization. For example, very often, users have to carefully design the specifications of the problem to avoid instability in the optimizer. As such, extensive interactions between the ML and the user are required [27]. Our framework takes an important step towards solving the above problems.

In this article, a structure which allows using 2D simulation with cylindrical coordinate to capture full 3D effect is used. If the same framework is used for 3D simulation, it is expected that the simulation time can be increased up to 10 times, depending on the types of simulations and models involved. Thus, the time needed to perform data generation using TCAD can be as long as 20 days if using our current computation resources but can be significantly reduced with enhanced computation capability. Moreover, by choosing the TCAD models appropriately (such as using a simplified model with similar accuracy as in [30]) or using innovative methodologies to perform 3D simulations (such as mixed-mode simulations with multiple 2D slices as in [31]), the simulation time can be reduced substantially.

VI. CONCLUSION

An ML-TCAD framework is proposed and demonstrated for device variation and operating condition analysis, which can extract the key material and device parameters and operating conditions (such as ambient temperature) from the device I-V characteristics and identify the major root cause for the variation in device I-V characteristics. Using Ga_2O_3 SBD as a case study, it is shown that our framework can predict the physical parameters in agreement with experimental results. The ML algorithm demonstrated in this work is the Principal Component Analysis (PCA) followed by third order polynomial regression. PCA on the input I-V curves was found to be critical for increasing the robustness of ML, which allows for effective prediction without physical quantities extraction, even when the experimental data is very noisy. It demonstrates the potential of the TCAD-ML framework for relaxing the need for the extensive and costly device and material characterizations in the device variation and operating temperature analysis. Moreover, since no physical quantities extraction is required and only simple 3rd polynomial regression and PCA are needed, such a method is readily transferrable to solve other problems such as defect identification using Capacitance-Voltage (*C-V*) curves of other devices.

ACKNOWLEDGMENT

The authors thank Dr. Pooya Jannaty of Cruise and Dr. Philip Leong of the University of Sydney for the discussion of ML algorithms. The experimental work is in part supported by the Southeastern Center for Electrical Engineering Education program and the High Density Integration industry mini-consortium of the Center for Power Electronics Systems at Virginia Tech.

REFERENCES

[1] G. A. Susto, M. Terzi, and A. Beghi, "Anomaly detection approaches for semiconductor manufacturing," *Procedia Manuf.*, vol. 11, pp. 2018–2024, Sep. 2017, doi: 10.1016/j.promfg.2017.07.353.

[2] D. Ding, X. Wu, J. Ghosh, and D. Z. Pan, "Machine learning based lithographic hotspot detection with critical-feature extraction and classification," in *Proc. IEEE Int. Conf. IC Design Technol.*, Austin, TX, USA, 2009, pp. 219–222, doi: 10.1109/ICICDT.2009.5166300.

[3] R. Luo, "Optical proximity correction using a multilayer perceptron neural network," *J. Opt.*, vol. 15, Jun. 2013, Art. no. 075708, doi: 10.1088/2040-8978/15/7/075708.

[4] Y. S. Bankapalli and H. Y. Wong, "TCAD augmented machine learning for semiconductor device failure troubleshooting and reverse engineering," in *Proc. Int. Conf. Simulat. Semicond. Process. Devices (SISPAD)*, Udine, Italy, 2019, pp. 21–24, doi: 10.1109/SISPAD.2019.8870467.

[5] C.-W. Teo, K. L. Low, V. Narang, and A. V.-Y. Thean, "TCAD-enabled machine learning defect prediction to accelerate advanced semiconductor device failure analysis," in *Proc. Int. Conf. Simulat. Semicond. Process. Devices (SISPAD)*, Udine, Italy, 2019, pp. 17–20, doi: 10.1109/SISPAD.2019.8870440.

[6] H. Carrillo-Nuñez, N. Dimitrova, A. Asenov, and V. Georgiev, "Machine learning approach for predicting the effect of statistical variability in Si junctionless nanowire transistors," *IEEE Electron Device Lett.*, vol. 40, no. 9, pp. 1366–1369, Sep. 2019, doi: 10.1109/LED.2019.2931839.

[7] J. Chen *et al.*, "Powernet: SOI lateral power device breakdown prediction with deep neural networks," *IEEE Access*, vol. 8, pp. 25372–25382, 2020, doi: 10.1109/ACCESS.2020.2970966.

[8] A. C. Müller and S. Guido, *Introduction to Machine Learning With Python: A Guide for Data Scientists*. Beijing, China: O'Reilly, 2017.

[9] J. Thipakorn, R. Waranusast, and P. Riyamongkol, "Egg weight prediction and egg size classification using image processing and machine learning," in *Proc. 14th Int. Conf. Elect. Eng./Electron. Comput. Telecommun. Inf. Technol. (ECTI-CON)*, Phuket, Thailand, 2017, pp. 477–480, doi: 10.1109/ECTICon.2017.8096278.

[10] A. Asenov, "Statistical device variability and its impact on design," in *Proc. 14th IEEE Int. Symp. Asynchronous Circuits Syst.*, Newcastle upon Tyne, U.K., 2008, pp. 15–16, doi: 10.1109/ASYNC.2008.9.

[11] M. Higashiwaki and G. H. Jessen, "Guest editorial: The dawn of gallium oxide microelectronics," *Appl. Phys. Lett.*, vol. 112, no. 6, Feb. 2018, Art. no. 060401, doi: 10.1063/1.5017845.

[12] S. J. Pearton *et al.*, "A review of Ga_2O_3 materials, processing, and devices," *Appl. Phys. Rev.*, vol. 5, no. 1, Jan. 2018, Art. no. 011301, doi: 10.1063/1.5006941.

[13] B. Wang *et al.*, "High-voltage vertical Ga_2O_3 power rectifiers operational at high temperatures up to 600 K," *Appl. Phys. Lett*. vol. 115, Dec. 2019, Art. no. 263503. [Online]. Available: https://doi.org/10.1063/1.5132818

[14] N. Allen *et al.*, "Vertical Ga_2O_3 schottky barrier diodes with small-angle beveled field plates: A baliga's figure-of-merit of 0.6 GW/cm^2," *IEEE Electron Device Lett.*, vol. 40, no. 9, pp. 1399–1402, Sep. 2019, doi: 10.1109/LED.2019.2931697.

[15] J. Yang, Z. Sparks, F. Ren, S. J. Pearton, and M. Tadjer, "Effect of surface treatments on electrical properties of β-Ga_2O_3," *J. Vac. Sci. Technol. B*, vol. 36, no. 6, Nov. 2018, Art. no. 061201, doi: 10.1116/1.5052229.

[16] *Sentaurus^{TM} Device User Guide Version O-2018.06*, Synopsys, Inc.,. Mountain View, CA, USA, Jun. 2018.

[17] D. B. M. Klaassen, "A unified mobility model for device simulation—I. Model equations and concentration dependence," *Solid-State Electron.*, vol. 35, no. 7, pp. 953–959, 1992, doi: 10.1016/0038-1101(92)90325-7.

[18] K. Goto *et al.*, "Halide vapor phase epitaxy of Si doped β-Ga2O3 and its electrical properties," *Thin Solid Films*, vol. 666, pp. 182–184, Nov. 2018, doi: 10.1016/j.tsf.2018.09.006.

[19] A. T. Neal *et al.*, "Donors and deep acceptors in β-Ga_2O_3," *Appl. Phys. Lett.*, vol. 113, Aug. 2018, Art. no. 062101, doi: 10.1063/1.5034474.

[20] N. Moser *et al.*, "Ge-doped b-Ga_2O_3 MOSFETs," *IEEE Electron Device Lett.*, vol. 38, no. 6, pp. 775–778, Jun. 2017, doi: 10.1109/LED.2017.2697359.

[21] Z. Guo *et al.*, "Anisotropic thermal conductivity in single crystal β-gallium oxide," *Appl. Phys. Lett.*, vol. 106, Mar. 2015, Art. no. 111909, doi: 10.1063/1.4916078.

[22] D. Splith *et al.*, "Determination of the mean and the homogeneous barrier height of Cu Schottky contacts on heteroepitaxial ß-Ga_2O_3 thin films grown by pulsed laser deposition," *Phys. Status Solidi*, vol. 211, no. 1, pp. 40–47, 2014, doi: 10.1002/pssa.201330088.

[23] G. Jian *et al.*, "Characterization of the inhomogeneous barrier distribution in a Pt/(100)β-Ga_2O_3 Schottky diode via its temperature-dependent electrical properties," *AIP Adv.*, vol. 8, Jan. 2018, Art. no. 015316, doi: 10.1063/1.5007197.

[24] *Sentaurus^{TM} Structure Editor User Guide Version O-2018.06*, Synopsys, Inc., Mountain View, CA, USA, Jun. 2018.

[25] A. Das *et al.*, "An advanced MOSFET design approach and a calibration methodology using inverse modeling that accurately predicts device characteristics," in *Int. Electron Devices Meeting Tech. Dig.*, Washington, DC, USA, pp. 687–690, 1997, doi: 10.1109/IEDM.1997.650476.

[26] Z. K. Lee, M. B. McIlrath, and D. A. Antoniadi, "Inverse modeling of MOSFETs using I-V characteristics in the subthreshold region," in *Int. Electron Devices Meeting Tech. Dig.*, Washington, DC, USA, 1997, pp. 683–686, doi: 10.1109/IEDM.1997.650475.

[27] S. Holzer, A. Sheikoleslami, S. Wagner, C. Heitzinger, T. Grasser, and S. Selberherr, "Optimization and inverse modeling for TCAD applications," in *Proc. Symp. Nano Devices Technol.* Hsinchu, Taiwan, 2004, p. 113–116.

[28] R. Strasser, R. Plasun, and S. Selberherr, "Practical inverse modeling with SIESTA," in *Proc. Int. Conf. Simulat. Semicond. Process. Devices*, Kyoto, Japan, Sep. 1999, pp. 91–94, doi: 10.1109/SISPAD.1999.799268.

[29] S. Molesky, Z. Lin, A. Y. Piggott, W. Jin, J. Vucković, and A. W. Rodriguez, "Inverse design in nanophotonics," *Nat. Photon.*, vol. 12, pp. 659–670, Nov. 2018, doi: 10.1038/s41566-018-0246-9.

[30] H.-Y. Wong, D. Dolgos, L. Smith, and R. V. Mickevicius, "Modified Hurkx band-to-band-tunneling model for accurate and robust TCAD simulations," *Microelectron. Rel.*, vol. 104, Jan. 2020, Art. no. 113552.

[31] F. Nallet, L. Silvestri, T. Cilento, C. Yun, S. Holland, and M. Röver, "TCAD simulation methodology for electrothermal analysis of discrete devices including package," in *Proc. IEEE 26th Int. Symp. Power Semicond. Devices IC's (ISPSD)*, Waikoloa, HI, USA, 2014, pp. 334–337, doi: 10.1109/ISPSD.2014.6856044.